RSC Advances

PAPER

View Article Online
View Journal | View Issue

Cite this: *RSC Adv.*, 2024, **14**, 12397

Surface modification of halide perovskite using EDTA-complexed SnO_2 as electron transport layer in high performance solar cells†

Nuno Marques, Santanu Jana, Manuel J. Mendes, Hugo Águas, Rodrigo Martins and Shrabani Panigrahi *

Received 27th December 2023
Accepted 8th April 2024

DOI: 10.1039/d3ra08900b

rsc.li/rsc-advances

The long-term performance of metal halide perovskite solar cells (PSCs) can be significantly improved by tuning the surface characteristics of the perovskite layers. Herein, low-temperature-processed ethylenediaminetetraacetic acid (EDTA)-complexed SnO_2 (E-SnO_2) is successfully employed as an electron transport layer (ETL) in PSCs, enhancing the efficiency and stability of the devices. The effects of EDTA treatment on SnO_2 are investigated for different concentrations: comparing the solar cells' response with 15%–2.5% SnO_2 and E-SnO_2 based ETLs, and it was found that 7.5% E-SnO_2 provided the best results. The improved surface properties of the perovskite layer on E-SnO_2 are attributed to the presence of small amount of PbI_2 which contributes to passivate the defects at the grain boundaries and films' surface. However, for the excess PbI_2 based devices, photocurrent dropped, which could be attributed to the generation of shallow traps due to excess PbI_2. The better alignment between the Fermi level of E-SnO_2 and the conduction band of perovskite is another favorable aspect that enables increased open-circuit potential (V_{OC}), from 0.82 V to 1.015 V, yielding a stabilized power conversion efficiency of 15.51%. This complex ETL strategy presented here demonstrates the enormous potential of E-SnO_2 as selective contact to enhance the perovskite layer properties and thereby allow stable and high-efficiency PSCs.

Introduction

The emerging development of perovskite solar cells (PSCs) has been leading to exciting research in the field of photovoltaics in the past decade due to the PSCs' high solar-to-electric power conversion efficiency (PCE),[1,2] low fabrication cost,[3–5] band gap tunning capability,[6] small exciton energy,[7,8] excellent bipolar carrier transport, long charge diffusion length[9] *etc.* Recent research efforts on new perovskite compositions, thin film growth, interfacial engineering and device architectures have resulted in remarkable PCEs ~ 26% for single junction PSCs.[10] The typical configuration of n-i-p structured PSCs usually consists of a glass substrate with a transparent conducting oxide (TCO) layer, followed by an n-type electron transport layer (ETL), a perovskite absorber layer, a p-type hole transport layer (HTL), and finally a metal contact.

The ETL is a crucial component in PSCs, as it significantly influences the photovoltaic performance and charge dynamics of the device.[11–13] For a device to work well, the ETL should meet some fundamental requirements: good optical transmittance to ensure that enough light is transmitted to the perovskite absorber, well matched energy level with perovskite materials to provide the desired open-circuit voltage (V_{OC}), and a high electron mobility to efficiently remove carriers from the active layer to prevent charge recombination *etc.* Currently, nearly all PSCs with high PCE are based on mesoporous-type architecture,[14,15] which frequently require high temperatures to sinter the mesoporous layer for optimal performance, compromising its low-cost advantage and limiting its application in flexible and tandem devices. On the other hand, planar-type PSCs consisting of stacked planar thin films have been developed using low-temperature and low-cost synthesis techniques. Compared to the more conventional TiO_2, SnO_2 is a more promising ETL candidate for highly efficient PSCs due to its higher transmittance, large bandgap (3.6–4.5 eV), superior optical and electric properties, band alignment with perovskite, and exceptional stability in the presence of moisture, heat, and light with negligible photoactivity.[16] The lower conduction band and higher carrier mobility (240 cm^2 (V^{-1} s^{-1})) of SnO_2 leads to a more effective carrier transport.[11,17]

A number of methods, including spin-coating after solution processing, chemical bath deposition (CBD),[18] atomic layer deposition (ALD),[19] electrochemical deposition (ED)[20] *etc.* have been utilized to produce low-temperature SnO_2 films. For the

CENIMAT|i3N, Department of Materials Science, School of Science and Technology, NOVA University Lisbon and CEMOP/UNINOVA, Campus de Caparica, Caparica, 2829-516, Portugal. E-mail: s.panigrahi@campus.fct.unl.pt

† Electronic supplementary information (ESI) available. See DOI: https://doi.org/10.1039/d3ra08900b

first time in conventional planar-type PSCs, Ke *et al.*[21] employed SnO_2 thin film as an ETL and demonstrated a PCE of 16.02% with improved hysteresis. Afterwards, different types of SnO_2 thin films have been investigated in PSCs, such as SnO_2 nanostructured in different forms and SnO_2 QDs.[22–24] However, due to defects at the interfaces of perovskite and SnO_2, a degradation on the PSCs' performance has been observed. This has been attributed to charge buildup at the ETL/perovskite interface, which is caused by the ETL's low electron mobility. On the other hand, self-doped defects on the surface of SnO_2 (like Sn and O vacancies, surface hydroxyls, and others) have a big effect on the performance as well as on the stability of PSCs.[25,26] In more detail, hydroxyl groups (–OH) and dangling bonds on the surface of SnO_2 reduce the energy required to form oxygen vacancies and facilitate oxygen diffusion towards the perovskite lattice.[27] Therefore, elemental doping,[28–31] bilayer design,[32,33] and interface modification[11,34–36] on the SnO_2 film were widely employed to enhance the performance of PSCs. Yang *et al.*[37] employed an ETL composed of SnO_2 complexed with ethylenediaminetetraacetic acid (EDTA) and showed that the Fermi level of EDTA-complexed SnO_2 is better matched with the conduction band of the perovskite layer compared to conventional SnO_2 ETL. It revealed the simultaneous advantages of hysteresis suppression and high V_{OC}. These results represent a significant advancement in the development of high-performance PSCs and pave the way for further improvements in device efficiency and stability. Gong *et al.*[38] reported the impact of the surface modification for SnO_2 ETL on the stability and interfacial physicochemical characteristics of PSC devices. The addition of NH_4F solution has the potential to modify the morphology of the SnO_2 film, resulting in the filling of pinholes and cracks and the formation of a uniform and uninterrupted layer for the high performance PSCs.[39] Keshtmand *et al.*[40] reported the treatment of NH_4Cl to modify the surface of SnO_2 ETL to enhance the efficiency of planar PSCs, specifically in terms of open-circuit voltage (V_{OC}). Muthukrishnan *et al.*[41] applied oxygen plasma treatment to improve the quality of low-temperature processed SnO_2 ETL to enhance the PSCs' efficiency. Cao *et al.*[42] modified the surface defects of SnO_2 ETL in PSCs by applying a fullerene derivative. As a result, the authors demonstrated an increase in electron transport and a reduction in charge recombination velocity, resulting in a highly efficient PSC with a PCE of 21.39%.

In this work, we adopt a simple and effective treatment by adding EDTA to commercially available SnO_2 aqueous colloids. The objective is to modify the surface of SnO_2 particles to enhance the stability of industrial SnO_2 colloidal films, which serve as ETL in our PSCs. Here, EDTA treated SnO_2 is denoted as E-SnO_2. We have also conducted a comprehensive investigation by varying the concentration (15%–2.5%) of commercially available SnO_2 and its EDTA-complexed counterpart (E-SnO_2). Unlike previous studies, which often focused solely on one aspect of device optimization, our approach allowed us to simultaneously explore the properties of the resulting perovskite layers, and the performance of the corresponding best devices across a wide range of SnO_2 and E-SnO_2 concentrations. Due to its powerful chelation activity, EDTA offers good ETL modification in organic solar cells.[43] The material characteristics of low-temperature treated E-SnO_2 are comparable to those of high-temperature annealed SnO_2. Therefore, E-SnO_2 ETL-based PSCs exhibit a substantial enhancement in PCE, in comparison to the standard SnO_2 ETL-based PSCs, due to enhancement in V_{OC} and fill factor (FF). Moreover, E-SnO_2 ETL aids to moderate the perovskite film by increasing the grain size and changing the surface potential, which can strongly reduce the charge recombination. Besides, E-SnO_2 possesses high electron mobility, which facilitates the movement of electrons. However, the carrier extraction was possibly affected by the introduction of shallow traps for E-SnO_2 ETL-based devices, upon excess presence of PbI_2 in the perovskite film, resulting in a decrease of the short-circuit current. Overall, the investigation revealed that 7.5% E-SnO_2 yielded the most favorable outcomes and the PCE for PSCs based on E-SnO_2 ETL increased from 13.20% to 15.51%, relative to the control SnO_2 based PSC. For prospective applications, this study demonstrates a promising route for the development of low-temperature fabricated PSCs with attractive cost-effectiveness.

Results and discussion

Fig. 1(a) and (b) show the schematic representation of the perovskite film formation on SnO_2 and E-SnO_2 ETLs, respectively. The ETLs were first deposited on glass/ITO substrate by spin-coating technique. After the annealing treatment, perovskite solution was then spun onto the ETL surface. Details of the experimental part are presented in the next section. Fig. 1(a) and (b) show the perovskite surface with large grains, however, the perovskite film on E-SnO_2 show the similar morphology with PbI_2 distributed into the GBs and on the surfaces of the perovskite film. To know the topological information of the perovskite films in greater depth, scanning electron microscopy (SEM) was conducted to compare the films morphology. To make SnO_2 solutions with varying concentrations, the purchased SnO_2 aqueous colloidal dispersion (15 wt%) was diluted with deionized water to achieve different concentrations of 10, 7.5, and 2.5 wt%. Simultaneously, E-SnO_2 solutions were prepared by mixing EDTA solution with SnO_2 colloidal solution in a proper ratio.

The details of the preparation technique are described in the experimental section. Fig. 2(a) shows the surface morphology of the perovskite film on only SnO_2 (15%) based ETL. Fig. 2(b)–(e) show the SEM images of the perovskite films on E-SnO_2 (15%), E-SnO_2 (10%), E-SnO_2 (7.5%) and E-SnO_2 (2.5%), respectively. It is observed that for the E-SnO_2 based perovskite film, the pinholes in between the grains slowly decreased with decreasing the concentration of E-SnO_2 and the appearance of PbI_2 at the grain boundary and surfaces of the perovskite films. In the field of lead halide perovskite, SEM is typically optimized for the detection of secondary electrons, which convey only topological information. However, a portion of electrons that have been backscattered will also be detected, providing compositional information. The intensity of backscattered electrons is proportional to the average

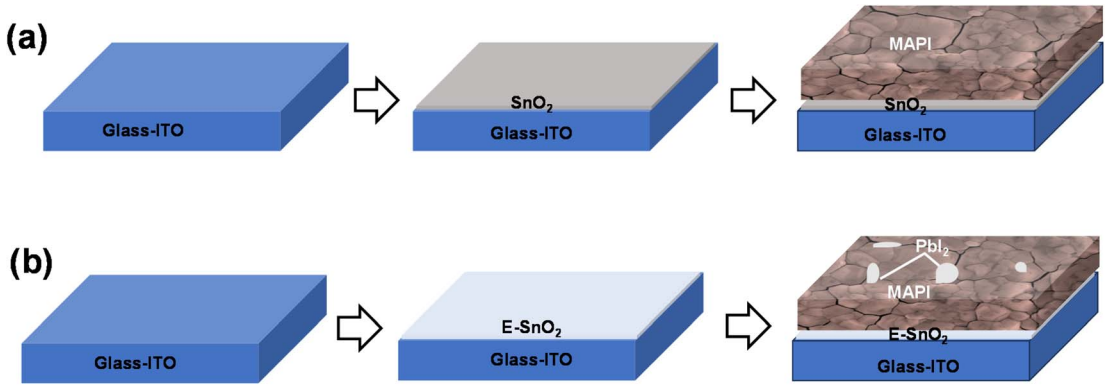

Fig. 1 Schematic diagrams of perovskite film fabrication procedures: (a) on SnO_2 ETL, (b) E-SnO_2 ETL.

atomic number of the atoms in the sample, with regions with a higher average atomic number appearing brighter in typical images.[44] As the average atomic number of PbI_2 is higher than that of the $MAPbI_3$ perovskite around it, therefore, bright PbI_2 crystals can be seen on the surfaces of the perovskite films in Fig. 2(b)–(d), respectively. Because PbI_2 (marked with white open circle) has a different contrast compared to perovskite grains.

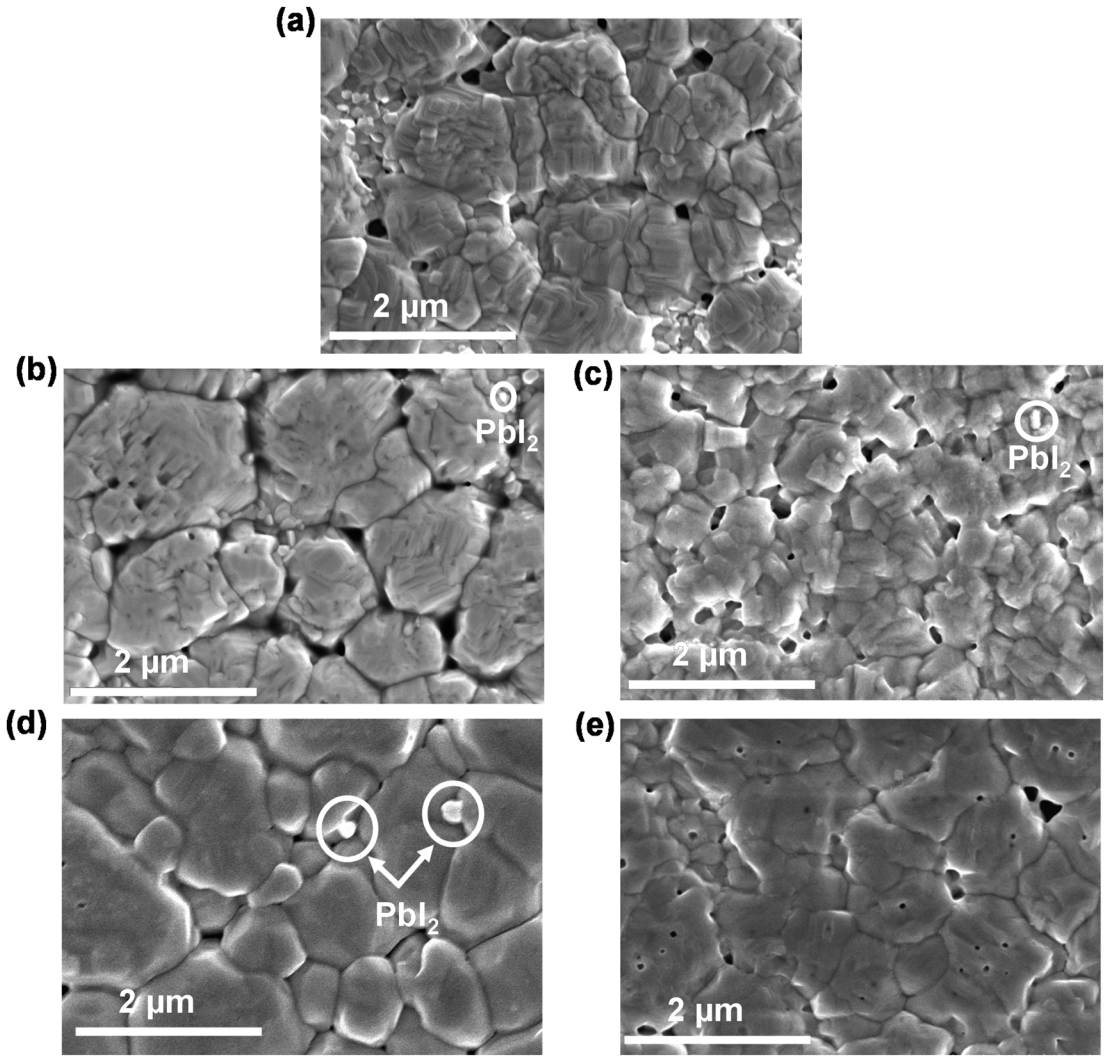

Fig. 2 Surface morphology (FESEM image) of the perovskite films on (a) SnO_2 (15%), (b) E-SnO_2 (15%), (c) E-SnO_2 (10%), (d) E-SnO_2 (7.5%) and (e) E-SnO_2 (2.5%) ETLs.

Furthermore, X-ray diffraction (XRD) analysis is the most used method to detect the presence of crystalline PbI_2 in a perovskite film. Fig. 3(a) shows the combined XRD pattern for perovskite films on SnO_2 (15%), E-SnO_2 (15%), E-SnO_2 (10%), E-SnO_2 (7.5%) and E-SnO_2 (2.5%), respectively. In case of only SnO_2 based perovskite film, the peaks correspond to the tetragonal phase of $MAPbI_3$. However, the extra (001) diffraction peak for hexagonal PbI_2 at $2\theta = 12.6°$ is clearly observed for all E-SnO_2 based perovskite films. The zoom view for the PbI_2 peak clearly shows that the intensity is maximum for the 7.5% E-SnO_2 based perovskite films. The intensity of the crystalline (001) PbI_2 peak increases monotonically up to 7.5% and then starts to decrease when the concentration of E-SnO_2 solution decreases after that. X-ray photoelectron spectroscopy (XPS) was used to examine the surface chemical composition of the perovskite films (MAPI) on different ETLs to determine the origin of the alterations in crystalline structure. Fig. 3(b) shows the full XPS spectra for only the perovskite films deposited on SnO_2 (7.5%) and E-SnO_2 (7.5%) ETLs, respectively. These spectra show the four main peaks centered at 138 eV, 286 eV, 402 eV and 619 eV, which were assigned to Pb 4f, C 1s, N 1s and I 3d, respectively. The high resolution XPS spectra for Pb 4f and I 3d peaks are shown in Fig. 3(c) and (d), respectively. For only SnO_2 based MAPI film, the peaks of Pb $4f_{5/2}$ and Pb $4f_{7/2}$ were detected at 143.5 eV and 138.5 eV, respectively. For E-SnO_2 based ETL, the Pb 4f peak pairs shifted to a slightly lower binding energy. A decrease in binding energy results from an increase in the electron screening effect as a result of an increase in electron density.[45] This redshift in the binding energy can therefore be tentatively attributed to the interactions between uncoordinated PbI_2 and the electron-rich N and O atoms, which increase the electron cloud density and decrease the electron affinity of PbI_2 ions.[46]

The UV-visible spectra provide information about the influence of EDTA on the optical properties of MAPI films. The UV-visible spectra for all samples show a typical $MAPbI_3$ absorbance, with a peak at 747 nm. When compared to only SnO_2 based MAPI film, E-SnO_2 based MAPI films showed similar absorption with a slightly higher optical absorption intensity, as shown in Fig. 4(a). For the perovskite film on E-SnO_2 (7.5%), the intensity is much higher than others. This result is attributable to the increased crystallinity of the perovskite film due to E-SnO_2 ETL. Steady-state photoluminescence (PL) was also used to examine the recombination kinetics of the perovskite films formed on with and without EDTA based ETLs. Fig. 4(b) displays the respective PL spectra of the perovskite films on SnO_2 and E-SnO_2 based ETLs. All the films demonstrate a prominent emission peak at around 782 nm, which corresponds to the radiative recombination process from the valence band to the conduction band of perovskite under an excitation wavelength of 400 nm. Notably, a significantly decreased PL intensity is observed for the perovskite films deposited on E-SnO_2 than that for SnO_2 based perovskite films. The presence of PbI_2 at the E-SnO_2 based perovskite film surfaces and GBs might reduce the deep defects, thus resulting in reduced carrier recombination.[47,48]

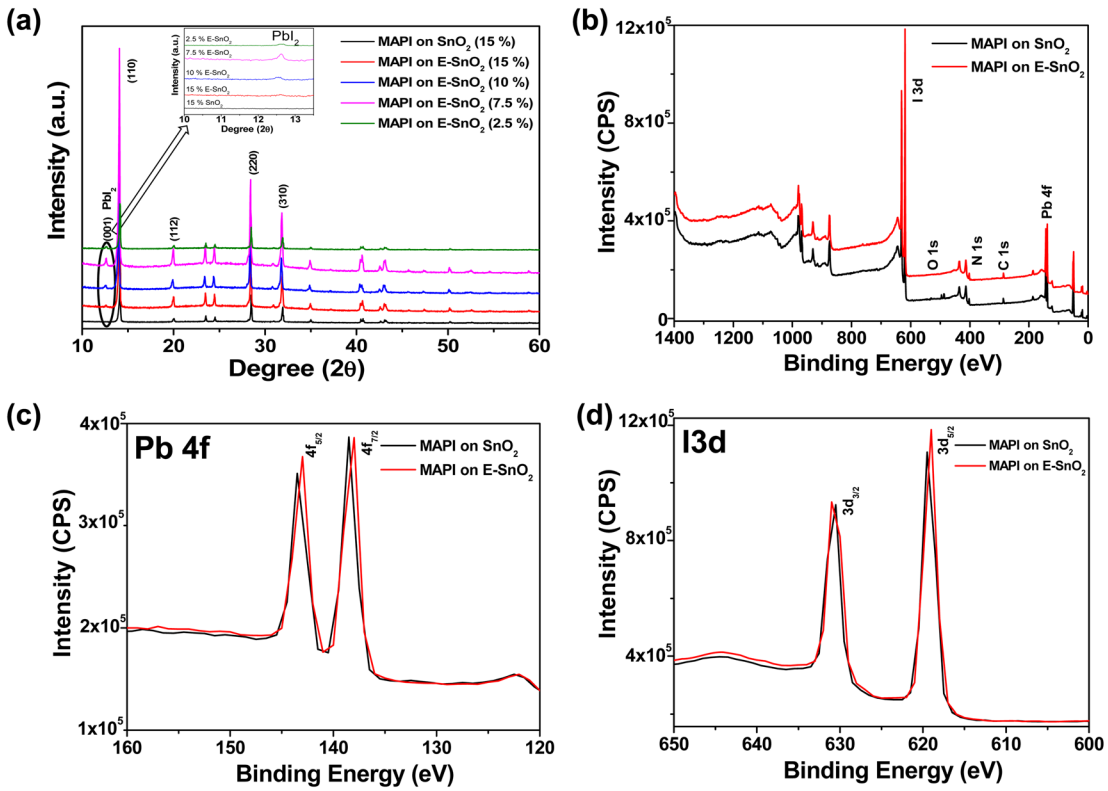

Fig. 3 (a) X-ray diffraction (XRD) pattern of the perovskite films on different ETLs. Zoom view of the PbI_2 peak only (Inset). (b) XPS survey spectra of the perovskite films deposited on SnO_2 and E-SnO_2 ETLs. XPS spectra for only (c) Pb 4f and (d) I 3d peaks.

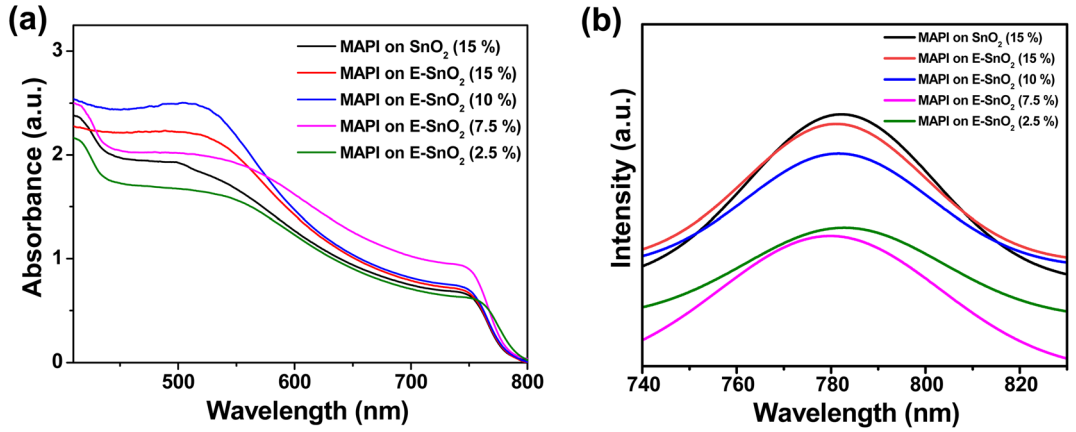

Fig. 4 (a) Absorbance and (b) steady-state PL spectra of perovskite films with various ETLs.

To characterize the effect of E-SnO_2 ETLs on perovskite device performance, PSCs were fabricated using the structure of ITO/SnO_2 (E-SnO_2)/MAPI/spiro-MeOTAD/Au as shown in Fig. 5(a). The cross-sectional SEM image for the corresponding solar cell is shown in Fig. 5(b) with each layer identified for a clearer understanding. The current density–voltage (J–V) curves are used to demonstrate how the device's performance gets better when the combined EDTA based ETL is utilized as a charge transporting layer. We choose only one concentration (7.5%) based ETL which shows the best device performance. The J–V curves for the PSCs with SnO_2 (7.5%) and E-SnO_2 (7.5%) based ETLs are shown in Fig. 5(c). The electrical measurement of the PSCs shows the values of open-circuit potential (V_{OC}) = 0.82 and 1.015 V, short-circuit current density (J_{SC}) = 24.31 and 22.16 mA cm^{-2} and fill factor (FF) = 66.5 and 69 for two different cases leading to a PCE of 13.25 and 15.51%, respectively. The improved PCE of the solar cell composed of E-SnO_2 is primarily attributed to the enhancement of V_{OC}. This increased V_{OC} from 0.82 V to 1.015 V (~200 mV) can be explained by the surface passivation that took place after using the EDTA based ETL. The J_{SC} value experiences a decreased value after using E-SnO_2 ETL confirmed by the corresponding EQE spectra in

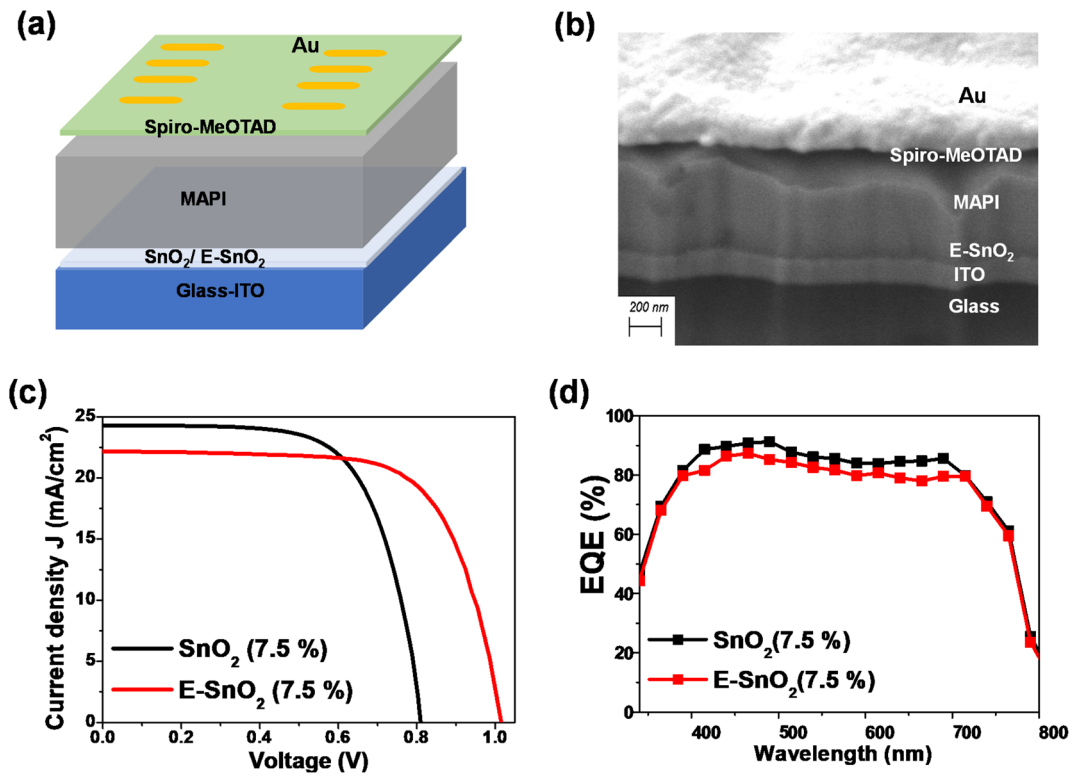

Fig. 5 (a) Schematic diagram for the device structure of the PSC. (b) The cross-section SEM image of the PSC on E-SnO_2 ETL. (c) Current density–voltage (J–V) curves for the PSCs on SnO_2 (7.5%) and E-SnO_2 (7.5%) ETLs. (d) Corresponding EQE curves for those cells.

Fig. 5(d). The calculation for the J_{SC} values from the EQE spectra is shown in Fig. S1 (ESI†). The stability graph for normalized PCE for both PSCs is shown in Fig. S2.† It shows that after 700 h, the PCE of the E-SnO_2 based solar cell decreased ~17%, while for the SnO_2 only based solar cell it decreased ~38%, which indicates an increase in stability with applying EDTA treatment. Fig. S3† depicts the *J–V* characteristics for both the reverse and forward scans of the highest-performing PSCs utilizing SnO_2 and E-SnO_2 ETLs, highlighting the hysteresis behavior of the devices. Additionally, the inset tables provide the performance parameters, including V_{OC}, J_{SC}, FF and PCE for each device configuration. The reduction in hysteresis observed in PSCs employing E-SnO_2 as the ETL can be attributed to a lower density of defects at the interface between E-SnO_2 and the perovskite layer, compared to the SnO_2/perovskite interface. This improvement in interface quality is facilitated by the enhanced surface coverage of the perovskite layer achieved with the E-SnO_2 ETL. Fig. 6 shows the photovoltaic characteristics and the distribution of the measured photovoltaic parameters V_{OC}, J_{SC}, FF, and PCE from 10 cells for other different concentration based SnO_2 and E-SnO_2 based devices. The enhanced V_{OC} and FF for all concentration E-SnO_2 based solar cells demonstrate that the presence of small amount of excess PbI_2 aids for reducing the defects in the perovskite films which may enhance PSC performance.[49–51] For only 15% E-SnO_2 based devices, the average value of J_{SC} is higher than that for SnO_2 based devices. However, for other concentration, J_{SC} values for E-SnO_2 based devices are lower than the SnO_2 based devices which might be the cause of excess presence of PbI_2 in MAPI. Roose *et al.*[44] also observed that excess PbI_2 initially serves to passivate defects and enhance charge carrier dynamics, its photolytic degradation can lead to the creation of additional trap states, thereby offsetting the benefits of its presence. Calloni *et al.*[52] demonstrated that the surface of MAPI undergoes *in situ* formation of a PbI_2 layer during annealing and sputtering. The formation of a thin layer of PbI_2 at the crystal surface, which functions as a surface barrier to stop electron transfer from the perovskite film. Kiermasch *et al.*[53] also observed the same characteristics with enhanced lifetime values in solar cells due to bromine doping in $MAPbI_3$ layer. In this case, the effective charge carrier lifetime becomes longer due to a reduction in Shockley–Read–Hall (SRH) recombination. More likely, excess PbI_2 in MAPI lattice, acting as dopants for the lattice, creates shallow traps along the conduction band and partially trap the charge carriers, that decreased electron injection into ETL (Fig. S4†). For that reason, the release of charge carriers will slow down which probably reduces the current at short-circuit condition. Therefore, we draw the conclusion that there is a delicate balance between the advantageous and detrimental effects of excess PbI_2 in perovskite materials, underscoring the importance of carefully controlling its concentration and stability to optimize PSC performance.

To further discuss the above results and provide more insight about the morphology, roughness and conductivity of the ETLs, additional characterizations have been performed. Atomic force microscopy (AFM) topography images of SnO_2 (7.5%) and E-SnO_2 (7.5%) ETLs are shown in Fig. S5(a) and (b),† respectively. Using Gwyddion software and its row statistical function, we analyzed the surface profiles and calculated the average roughness for SnO_2 and E-SnO_2 films to be 29.38 nm and 7.38 nm, respectively

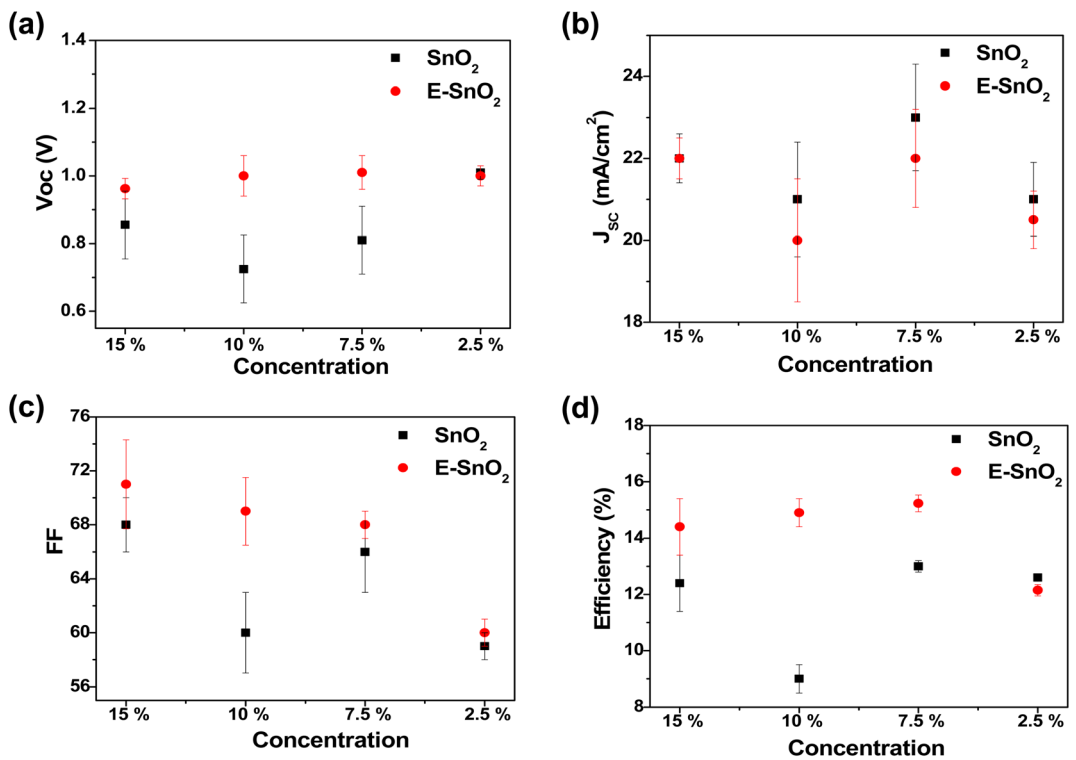

Fig. 6 The distribution of (a) V_{OC}, (b) J_{SC}, (c) FF and (d) PCE for different concentration ETL solution treated PSCs.

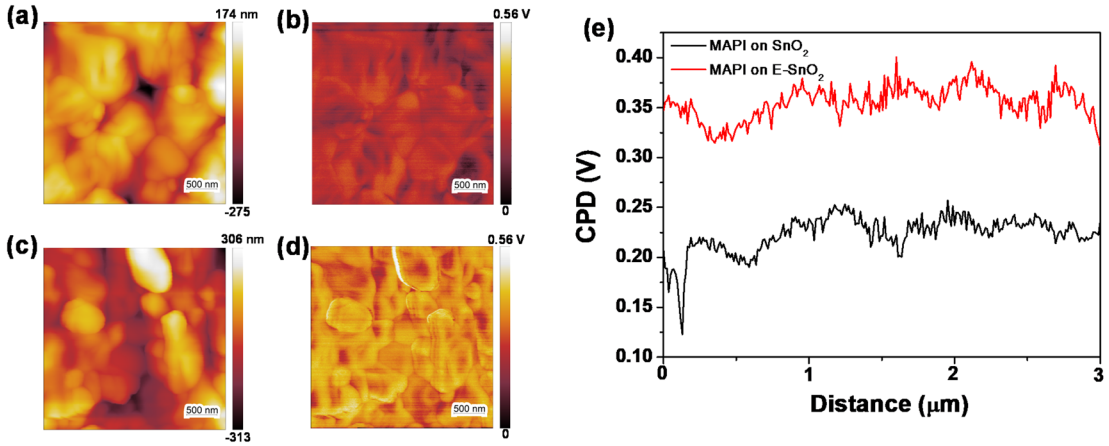

Fig. 7 (a and c) Topography and (b and d) corresponding surface potential images for the perovskite films on SnO_2 (7.5%) and E-SnO_2 (7.5%) ETLs, respectively. (e) Average CPD plot for the corresponding layers.

(Fig. S5c and d†). To know more about the statistical distribution of vertical fluctuations, we collected sixty distinct height profiles from various locations within the topographic images. These profiles were then compiled and utilized to construct plots wherein the width of the distribution corresponds to the surface roughness.[54–56] It was observed that the data points were broadly distributed over 11 nm for SnO_2, whereas for E-SnO_2 the distribution was slightly reduced to 9 nm (Fig. S5e and f†). This observation indicates that the EDTA treatment reduces the roughness of complex E-SnO_2 films. This reduction in roughness is a crucial factor in improving the formation of the perovskite layer on E-SnO_2, which is essential for achieving high-performance PSCs. In addition, we conducted Hall effect measurements on both types of ETLs to characterize its electron mobility. These measurements provide valuable insights into the charge carrier transport properties of the ETLs, which are critical for understanding its performance in PSCs. Table S1 (ESI†) shows that the E-SnO_2 film (7.5%) has an electron mobility of 140 $cm^3\ V^{-1}\ s^{-1}$, which is much higher than the electron mobility of SnO_2 only (36.8 $cm^3\ V^{-1}\ s^{-1}$). It is clear that the high electron mobility of E-SnO_2 facilitates the rapid transport of electrons within the ETL, enabling efficient extraction of photogenerated electrons from the perovskite layer. This helps minimize charge carrier losses and enhances overall device performance. Furthermore, to investigate the reason for the increased of V_{OC} in E-SnO_2 based solar cells, we have characterized the surface potentials of the perovskite layers for SnO_2 and E-SnO_2 based ETLs using Kelvin Probe Force Microscopy (KPFM). The KPFM tip moved easily across the surface of the perovskite layer, measuring the contact potential difference (CPD) between the tip and the sample. Olympus AC240TM probes (details in the experimental part) were used for KPFM measurements.[57,58] The AC tip voltage was set to 3 V in a double pass mode in air. The topography and the corresponding surface potential images of the perovskite layers are shown in Fig. 7. Fig. 7(a) and (c) show the topography images, while the corresponding surface potential images are shown in Fig. 7(b) and (d) for the perovskite layers on SnO_2 (7.5%) and E-SnO_2 (7.5%) ETLs, respectively. KPFM determines the CPD between the tip and sample surface by probing and nullifying the coulomb force between them (Fig. S6†). The CPD is equal to the difference of the work functions between the tip and sample. The quantity of trapped charge carriers at each layer's surface determines the surface potential. As shown by the average CPD plot (Fig. 7(e)) for the two cases, the surface work function of the perovskite film has been significantly modified by the treatment with EDTA. The perovskite on SnO_2 has an average potential difference of 230 mV, but the perovskite layer on E-SnO_2 has an average potential difference of 370 mV. The perovskite film with higher CPD value on E-SnO_2 indicates a reduction in the work function and a rise of the Fermi level, both of which are advantageous for the charge transfer process to separate photogenerated electron–hole pairs, which raises the V_{OC} and FF in PSCs. Therefore, the data presented in above suggests that EDTA treatment plays a crucial and favorable role in modifying the surface characteristics of MAPI, thus improving the functionality of PSCs; where, the current transport is slightly hampered for the excess PbI_2 based perovskite layers.

Conclusion

In this study, we presented a simple and useful strategy that employs EDTA treatment for the surface modification of SnO_2 ETL, capable of increasing the performance of planar PSCs. Low temperature deposited E-SnO_2 ETLs have shown to improve the properties of the perovskite layer deposited on top, resulting in enhanced PSC efficiency and stability.

The enlarged grain size of MAPI for E-SnO_2 ETL and the increased CPD values resulted in an improvement in V_{OC} from 0.82 V to 1.015 V, which was the main cause for the enhanced PSC performance. Our findings indicate that an adequate amount of PbI_2 in MAPI assists in passivating the polycrystalline film surfaces, owing to the advantageous Pb terminations decreasing the trap densities. Nevertheless, the drawbacks of excessive PbI_2 are also assessed. Namely the lower value of J_{SC} attained for the E-SnO_2 ETL based PSCs is likely caused by the introduction of shallow defects due to excess PbI_2

in MAPI, which decreases the carrier extraction probability from the absorber layer. Lastly, statistical data collected from PSCs showed that devices based on E-SnO_2 ETL also benefit from enhanced stability.

Experimental section

Materials

Glass/indium tin oxide (ITO) substrates; SnO_2 colloid precursor (15% H_2O colloidal dispersion); ethylenediaminetetraacetic acid (EDTA) were utilized for ETL. The MAPI perovskite solution was synthesized utilizing lead(II) iodide (PbI_2) and methylammonium iodide (CH_3NH_3I), dimethylformamide (DMF), and dimethyl sulfoxide (DMSO), all of which were obtained from Sigma-Aldrich. To prepare HTL, a solution of chlorobenzene (C_6H_5Cl) is mixed with 4-*tert*-butylpyridine (4-*t*BP, 96%, Sigma-Aldrich), bis(trifluoromethane) sulfonimide lithium salt (Li-TFSI) (Sigma-Aldrich), and Spiro-MeOTAD (Sigma-Aldrich). The solvents and compounds were utilized without additional purification or treatment.

Fabrication of SnO_2/E-SnO_2 layer and perovskite solar cell

The glass/ITO substrates were successively washed by sonication with soap solution, distilled water, acetone, and isopropanol after the etching process. The substrates were subsequently dried out using compressed air. In addition, the substrates experienced a 15 minute UV–ozone treatment before SnO_2/E-SnO_2 deposition. SnO_2 film is prepared by spin coating on cleaned ITO substrate at 4000 rpm for 30 s and then heated at a temperature of 150 °C for 15 min and 180 °C for 1 h. For making different concentration based SnO_2 solution, as purchased SnO_2 aqueous colloidal dispersion (15 wt%) was diluted using deionized water to the concentrations of 10, 7.5 and 2.5 wt%. The EDTA solution was prepared by dissolving 1 mg of EDTA in 5 mL of deionized water. Both solutions were stirred for 30 min at room temperature. The EDTA solution was mixed with the SnO_2 solutions with a volume ratio of 1 : 1 to obtain the E-SnO_2 solutions with the corresponding concentrations. These E-SnO_2 solutions were then stirred at 80 °C for 5 h. After that, E-SnO_2 solutions were spin coated on cleaned ITO substrates at 5000 rpm for 60 seconds and moved to a vacuum oven at 60 °C for 30 minutes to remove the leftover solvent.

Prior to the deposition of the perovskite layer, the samples experienced a 15 minute UV–ozone treatment at 150 °C. The spin coating technique was employed to deposit perovskite films in two stages: at 1000 and 5000 rpm for 10 and 30 seconds, respectively, and using a precursor solution combining PbI_2 and MAI (molar ratio 1 : 1) in anhydrous DMF and DMSO. 10 seconds prior to the end of the program, 150 μL of chlorobenzene was dropped onto the substrate in the second phase of the spinning condition. The samples were then annealed at 100 °C for 15 minutes. The HTL was subsequently formed on top of the perovskite layer by spin-coating technique at 3500 rpm for 30 seconds with the solution of Spiro-MeOTAD (40 μL) made with chlorobenzene, LiTFSI stock solution (520 mg of LiTFSI in 1 mL of acetonitrile), and 4-*t*BP. 100 nm of gold on top of the device was deposited using home made e-beam evaporation technology under high vacuum to operate as a cathode.

Characterizations

SEM (Carl Zeiss AURIGA Cross Beam workstation) and atomic force microscopy (AFM; MFP-3D Infinity atomic force microscope from Oxford Instruments Asylum Research; Santa Barbara, CA) were used to examine the surface morphology and topology of SnO_2/E-SnO_2 and MAPI layers. Cross-sectional SEM images for devices were obtained by employing a standard ET type secondary electron detector in conjunction with 30 kV Ga+ ions at 20 pA. We used Olympus AC240TM probes for KPFM in an Asylum Research MFP-3D standalone system. The spring constant was 2 N m^{-1}, the resonant frequency was 70 kHz, and the AC tip voltage was 3 V in a double pass mode. Using the Hall measurement system (BiO-RAD/Nanometrics HL5500), the carrier concentration of the different layers had been measured.

X-ray diffractometer (Panalytical Xpert PRO system; Cu Kα radiation; $\lambda = 1.5405$ Å and X'Celerator 1D detector) was used to know the crystallographic structure of the material. An AXIS Supra+ spectrometer by Kratos Analytical was used for X-ray photoelectron spectroscopy (XPS) examination. The steady-state photoluminescence (PL) spectra was acquired using a high-resolution spectrometer (Horiba Jobin Yvon, Model: iHR 320) together with a photomultiplier tube. The photovoltaic characteristics of PSCs were measured under AM 1.5G illumination using a workstation (Sciencetech SS1.6kW-A-2-Q system with Keithley source meter: Model 2400). A monochromator (Newport) and a Xenon lamp (Newport) were used to assess external quantum efficiency (EQE).

Conflicts of interest

There are no conflicts to declare.

Acknowledgements

This work is funded by FCT-MCTES (Fundação para a Ciência e Tecnologia, I. P.) *via* the postdoctoral grant SFRH/BPD/123502/2016, under the projects LA/P/0037/2020, UIDP/50025/2020 and UIDB/50025/2020 of the Associate Laboratory Institute of Nanostructures, Nanomodelling and Nanofabrication—i3N, and by the projects FlexSolar (PTDC/CTM-REF/1008/2020), SpaceFlex (2022.01610.PTDC) and M-ECO2 (Industrial cluster for advanced biofuel production, Ref. C644930471-00000041) co-financed by PRR - Recovery and Resilience Plan of the European Union (Next Generation EU). This work also received funding from the European Community's H2020 program under the projects DIGISMART (grant agreement no. 787410, ERC-2018-AdG) and SYNERGY (H2020-WIDESPREAD-2020-5, CSA, proposal no. 952169). We acknowledge Jonas Deuermeier and Tomás Calmeiro for their help in XPS and AFM measurements, respectively.

References

1 J. Y. Kim, J.-W. Lee, H. S. Jung, H. Shin and N.-G. Park, *Chem. Rev.*, 2020, **120**, 7867–7918.
2 J. Gong, Y. Cui, F. Li and M. Liu, *Small Sci.*, 2023, **3**, 2200108.
3 B. C. Karunarathne, S. P. Dunuweera, A. T. Medagedara, D. Velauthapillai, R. Punniamoorthy, A. G. U. Perera, L. A. DeSilva, K. Tennakone, R. M. G. Rajapakse and G. R. A. Kumara, *ACS Omega*, 2023, **8**, 23501–23509.
4 E. Couderc, *Nat. Energy*, 2017, **2**, 17080.
5 S. Panigrahi, S. Jana, T. Calmeiro, D. Nunes, J. Deuermeier, R. Martins and E. Fortunato, *J. Mater. Chem. A*, 2019, **7**, 19811–19819.
6 D. B. Straus and R. J. Cava, *ACS Appl. Mater. Interfaces*, 2022, **14**, 34884–34890.
7 M. C. Gélvez-Rueda, M. B. Fridriksson, R. K. Dubey, W. F. Jager, W. van der Stam and F. C. Grozema, *Nat. Commun.*, 2020, **11**, 1901.
8 K. R. Hansen, C. E. McClure, D. Powell, H.-C. Hsieh, L. Flannery, K. Garden, E. J. Miller, D. J. King, S. Sainio, D. Nordlund, J. S. Colton and L. Whittaker-Brooks, *Adv. Opt. Mater.*, 2022, **10**, 2102698.
9 G. W. P. Adhyaksa, L. W. Veldhuizen, Y. Kuang, S. Brittman, R. E. I. Schropp and E. C. Garnett, *Chem. Mater.*, 2016, **28**, 5259–5263.
10 J. Park, J. Kim, H. S. Yun, M. J. Paik, E. Noh, H. J. Mun, M. G. Kim, T. J. Shin and S. I. Seok, *Nature*, 2023, **616**, 724–730.
11 S. Panigrahi, M. Sk, S. Jana, S. Ghosh, J. Deuermeier, R. Martins and E. Fortunato, *ACS Appl. Energy Mater.*, 2022, **5**, 5680–5690.
12 S. Haque, M. J. Mendes, O. Sanchez-Sobrado, H. Águas, E. Fortunato and R. Martins, *Nano Energy*, 2019, **59**, 91–101.
13 S. Haque, M. Alexandre, C. Baretzky, D. Rossi, F. De Rossi, A. T. Vicente, F. Brunetti, H. Águas, R. A. S. Ferreira, E. Fortunato, M. Auf Der Maur, U. Würfel, R. Martins and M. J. Mendes, *ACS Photonics*, 2022, **9**, 2408–2421.
14 J. Wang, X. Zhou, J. Ni, J. Guan, M. Hu, R. Wang, Y. Zhang, J. Li, H. Cai and J. Zhang, *J. Mater. Sci.: Mater. Electron.*, 2021, **32**, 28417–28425.
15 S. Panigrahi, S. Jana, T. Calmeiro, D. Nunes, R. Martins and E. Fortunato, *ACS Nano*, 2017, **11**, 10214–10221.
16 S. Lin, B. Yang, X. Qiu, J. Yan, J. Shi, Y. Yuan, W. Tan, X. Liu, H. Huang, Y. Gao and C. Zhou, *Org. Electron.*, 2018, **53**, 235–241.
17 P. Sun, G. Qu, Q. Hu, Y. Ma, H. Liu, Z.-X. Xu and Z. Huang, *ACS Appl. Energy Mater.*, 2022, **5**, 3568–3577.
18 J. Zhang, C. Bai, Y. Dong, W. Shen, Q. Zhang, F. Huang, C. Bing and J. Zhong, *Chem. Eng. J.*, 2021, **425**, 131444.
19 S.-U. Lee, H. Park, H. Shin and N.-G. Park, *Nanoscale*, 2023, **15**, 5044–5052.
20 J.-Y. Chen, C.-C. Chueh, Z. Zhu, W.-C. Chen and A. Jen, *Sol. Energy Mater. Sol. Cells*, 2017, **164**, 47–55.
21 W. Ke, G. Fang, Q. Liu, L. Xiong, P. Qin, H. Tao, J. Wang, H. Lei, B. Li, J. Wan, G. Yang and Y. Yan, *J. Am. Chem. Soc.*, 2015, **137**, 6730–6733.
22 N. Chai, X. Chen, Z. Zeng, R. Yu, Y. Yue, B. Mai, J. Wu, L. Mai, Y.-B. Cheng and X. Wang, *Natl. Sci. Rev.*, 2023, **10**, nwad245.
23 K. Wei, J. Deng, L. Yang, C. Zhang, M. Huang, X. Cai, X. Zhang and J. Zhang, *Adv. Energy Mater.*, 2023, **13**, 2203448.
24 H. Wang, J. Yuan, J. Xi, J. Du and J. Tian, *J. Phys. Chem. Lett.*, 2021, **12**, 9142–9148.
25 J. Liu, S. Li, S. Liu, Y. Chu, T. Ye, C. Qiu, Z. Qiu, X. Wang, Y. Wang, Y. Su, Y. Hu, Y. Rong, A. Mei and H. Han, *Angew Chem. Int. Ed. Engl.*, 2022, **61**, e202202012.
26 E. Jiang, J. Yan, Y. Ai, N. Li, B. Yan, Y. Zeng, J. Sheng and J. Ye, *Mater. Today Energy*, 2019, **12**, 389–397.
27 J. Song, H. Liu, W. Pu, Y. Lu, Z. Si, Z. Zhang, Y. Ge, N. Li, H. Zhou, W. Xiao, L. Wang and M. Sui, *Energy Environ. Sci.*, 2022, **15**, 4836–4849.
28 Y. Qiang, Y. Xie, Y. Qi, P. Wei, H. Shi, C. Geng and H. Liu, *Sol. Energy*, 2020, **201**, 523–529.
29 R. Wang, J. Wu, S. Wei, J. Zhu, M. Guo, Q. Zheng, M. Wei and S. Cheng, *J. Power Sources*, 2022, **544**, 231870.
30 H. Zhou, Y. Yang, X. Li, S. Wu, J. Lu, S. Zhao, D. Wu, W. Xu, P. Chen and L. Zhou, *J. Lumin.*, 2023, **263**, 120144.
31 H. V. Quy and C. W. Bark, *ACS Omega*, 2022, **7**, 22256–22262.
32 H. Yi, D. Wang, M. A. Mahmud, F. Haque, M. B. Upama, C. Xu, L. Duan and A. Uddin, *ACS Appl. Energy Mater.*, 2018, **1**, 6027–6039.
33 X. Zhang, Y. Zhou, M. Chen, D. Wang, L. Chao, Y. Lv, H. Zhang, Y. Xia, M. Li, Z. Hu and Y. Chen, *Small*, 2023, **19**, 2303254.
34 T. Li, Y. Rui, X. Wang, J. Shi, Y. Wang, J. Yang and Q. Zhang, *ACS Appl. Energy Mater.*, 2021, **4**, 7002–7011.
35 V. Yarangsi, K. Hongsith, S. Sucharitakul, A. Ngamjarurojana, A. Tuantranont, P. Kumnorkaew, Y. Zhao, S. Phadungdhitidhada and S. Choopun, *J. Phys. D: Appl. Phys.*, 2020, **53**, 505103.
36 Y. Gao, Z. He, Q. Geng, X. Jia, S. Zhang and D. Wang, *J. Mater. Chem. C*, 2023, **11**, 14589–14596.
37 D. Yang, R. Yang, K. Wang, C. Wu, X. Zhu, J. Feng, X. Ren, G. Fang, S. Priya and S. Liu, *Nat. Commun.*, 2018, **9**, 3239.
38 M. A. Green, E. D. Dunlop, M. Yoshita, N. Kopidakis, K. Bothe, G. Siefer and X. Hao, *Prog. Photovolt. Res. Appl.*, 2023, **31**, 651–663.
39 R. Keshtmand, M. R. Zamani-Meymian, F. Mohamadkhani and N. Taghavinia, *Sol. Energy*, 2021, **228**, 253–262.
40 R. Keshtmand, M. R. Zamani-Meymian and N. Taghavinia, *Surf. Interfaces*, 2022, **28**, 101596.
41 A. P. Muthukrishnan, J. Lee, J. Kim, C. S. Kim and S. Jo, *RSC Adv.*, 2022, **12**, 4883–4890.
42 T. Cao, K. Chen, Q. Chen, Y. Zhou, N. Chen and Y. Li, *ACS Appl. Mater. Interfaces*, 2019, **11**, 33825–33834.
43 X. Li, X. Liu, W. Zhang, H.-Q. Wang and J. Fang, *Chem. Mater.*, 2017, **29**, 4176–4180.
44 B. Roose, K. Dey, Y.-H. Chiang, R. H. Friend and S. D. Stranks, *J. Phys. Chem. Lett.*, 2020, **11**, 6505–6512.
45 M. Zhu, Z. Sun, M. Fujitsuka and T. Majima, *Angew. Chem., Int. Ed.*, 2018, **57**, 2160–2164.
46 E. Khorshidi, B. Rezaei, D. Blätte, A. Buyruk, M. A. Reus, J. Hanisch, B. Böller, P. Müller-Buschbaum and T. Ameri, *Sol. RRL*, 2022, **6**, 2200023.

47 Q. Chen, H. Zhou, T.-B. Song, S. Luo, Z. Hong, H.-S. Duan, L. Dou, Y. Liu and Y. Yang, *Nano Lett.*, 2014, **14**, 4158–4163.
48 T. Du, C. H. Burgess, J. Kim, J. Zhang, J. R. Durrant and M. A. McLachlan, *Sustainable Energy Fuels*, 2017, **1**, 119–126.
49 K. Guo, *Energy Rep.*, 2023, **9**, 62–73.
50 A. Merdasa, A. Kiligaridis, C. Rehermann, M. Abdi-Jalebi, J. Stöber, B. Louis, M. Gerhard, S. D. Stranks, E. L. Unger and I. G. Scheblykin, *ACS Energy Lett.*, 2019, **4**, 1370–1378.
51 Z. Ahmad, R. A. Scheidt, M. P. Hautzinger, K. Zhu, M. C. Beard and G. Galli, *ACS Energy Lett.*, 2022, **7**, 1912–1919.
52 A. Calloni, A. Abate, G. Bussetti, G. Berti, R. Yivlialin, F. Ciccacci and L. Duò, *J. Phys. Chem. C*, 2015, **119**, 21329–21335.
53 D. Kiermasch, P. Rieder, K. Tvingstedt, A. Baumann and V. Dyakonov, *Sci. Rep.*, 2016, **6**, 39333.
54 K. Dey, S. Roy Chowdhury, E. Dykstra, H. P. Lu, R. Shinar, J. Shinar and P. Anzenbacher, *ACS Appl. Electron. Mater.*, 2021, **3**, 3365–3371.
55 K. Dey, S. R. Chowdhury, E. Dykstra, A. Koronatov, H. P. Lu, R. Shinar, J. Shinar and P. Anzenbacher, *J. Mater. Chem. C*, 2020, **8**, 11988–11996.
56 B. Dhital, V. G. Rao and H. P. Lu, *Phys. Chem. Chem. Phys.*, 2017, **19**, 17216–17223.
57 S. Panigrahi, T. Calmeiro, R. Martins, D. Nunes and E. Fortunato, *ACS Nano*, 2016, **10**, 6139–6146.
58 S. Panigrahi, S. Jana, T. Calmeiro, E. Fortunato, M. J. Mendes and R. Martins, *ACS Appl. Mater. Interfaces*, 2024, **16**, 1930–1940.